Depth sectioning using environmental and atomic-resolution STEM

Masaki Takeguchi[1*], Ayako Hashimoto[1], and Kazutaka Mitsuishi[1]

[1]Center for Basic Research on Materials, National Institute for Materials Science, 1-2-1 Sengen, Tsukuba, Ibaraki, 305-0047, Japan

*Correspondence should be addressed to

Masaki Takeguchi, Center for Basic Research on Materials, National Institute for Materials Science, 1-2-1 Sengen, Tsukuba, Ibaraki 305-0047, Japan

Phone: +81-29-859-2486

E-mail: TAKEGUCHI.Masaki@nims.go.jp

Running title: Depth sectioning technique

Keywords: Environmental, Liquid, Gas, Atomic resolution, STEM, Depth sectioning, 3D

Total Number of Pages: 41

Number of Figures: 8

Abstract

(Scanning) transmission electron microscopy (TEM) images of samples in gas and liquid media are acquired with an environmental cell (EC) via silicon nitride membranes. The ratio of sample signal against the background is a significant factor for resolution. Depth-sectioning Scanning TEM (STEM) is a promising technique that enhances the signal for a sample embedded in a matrix. It can increase the resolution to the atomic level, thereby enabling EC-STEM applications in important areas. This review introduces depth-sectioning STEM and its applications to high-resolution EC-STEM imaging of samples in gases and in liquids.

Abbreviations

TEM: Transmission electron microscopy

STEM: Scanning transmission electron microscopy

EC: Environmental cell

Introduction

Because an image acquired by transmission electron microscopy (TEM) or scanning TEM (STEM) is, to a good approximation, a two-dimensional projection of a sample, the relative contrast of internal structures or embedded particles in a thick matrix decreases as the thickness increases. Meanwhile, the need for three-dimensional (3D) nanometer- and atomic-scale imaging of nanocomposites, mesoporous materials, special-shaped nanomaterials, and nanoparticles distributed on support materials has been increasing. A combination of (S)TEM and computed tomography (i.e., (S)TEM tomography) has been the most practical method for 3D electron microscopy [1,2]. It enables 3D shapes and cross-sections to be visualized via computational 3D reconstructions from images acquired at different tilt angles. Because of sophisticated data acquisition and analyzing systems, (S)TEM tomography has been routinely used for 3D imaging. However, there exists a missing-cone problem caused by the limitation of the maximum tilt angle. The requirement of long exposure times is also a disadvantage. Finally, (S)TEM tomography requires dedicated sample holders designed for high tilt angles within the narrow gap of the objective lens. Therefore, it is difficult to perform (S)TEM tomography when using an environmental cell (EC) for sample observation in gas and liquid media.

Depth-sectioning STEM is an alternative 3D imaging technique [3-20]. It is capable of atomic resolution in a lateral direction, but the depth resolution is poor relative to (S)TEM tomography because of the vertically elongated STEM probe. A STEM image is formed via the convolution of a 3D object function and a 3D probe point spread function (PSF). Without spherical aberration correctors, the shape of a 3D probe function in conventional STEM is determined by the optimum convergence semi-angle that minimizes the sum of squares of an aperture aberration and a spherical aberration. Assuming that the spherical aberration coefficient C_s is equal to 1 mm, the optimum convergence semi-angle α is approximately 10 mrad, which yields a lateral probe dimension less than 0.2 nm and a vertical probe dimension greater than 50 nm [21]. State-of-the-art STEM instruments equipped with a spherical aberration corrector in a probe-forming lens can extend α to approximately 30 mrad or larger, thereby decreasing the vertical probe elongation to several nm [3-20].

This review discusses the 3D characteristics of depth-sectioning STEM using an aberration-corrected electron probe. The transferrable vertical frequency component of the 3D contrast transfer function depends on the lateral component. Depth sectioning is ineffective for objects primarily composed of low-frequency components (typically, laterally extended objects). The maximum depth resolution can be achieved when the object size is equivalent to the lateral size of the STEM probe. Measurements of 3D positions of dopant atoms as well as atomic-level surface topographies of thin films have been demonstrated [18]. Recent examples of depth-sectioning STEM for observing the dynamics of atomic-level structural changes of samples in gas and liquid media enclosed in an EC are also discussed [20, 43].

Theory

What determines the STEM probe sizes?

Hereafter, STEM refers to high-angle annular dark-field (HAADF)-STEM. What determines STEM probe sizes as STEM resolution is described as follows. The lateral (xy planes) size of STEM probe in geometrical optics, d_{xy}, is given by [22, 23]:

$$d_{xy} = \sqrt{\left(\frac{2}{\pi\alpha}\sqrt{\frac{I_p}{B}}\right)^2 + \left(\frac{1}{2}C_s\alpha^3\right)^2 + \left(0.6\frac{\lambda}{\alpha}\right)^2 + \left(C_c\alpha\frac{\Delta E}{E}\right)^2} \quad (1),$$

where the first, second, third, and fourth terms are probe sizes determined by the gun brightness, the spherical aberration, the aperture aberration (i.e., diffraction aberration), and the chromatic aberration, respectively. B is the gun brightness, α is the beam convergence semi-angle, I_p is the probe current, C_s is the spherical aberration coefficient, λ is the electron wavelength, C_c is the chromatic aberration coefficient, E is the electron energy, and ΔE is the energy spread. Astigmatism is omitted in Eq. (1). From the geometric approximation, the vertical dimension of the probe, d_z, corresponding to the STEM depth resolution, is estimated from [23, 24]:

$$d_z \approx \frac{d_{xy}}{\alpha} \approx \frac{\lambda}{\alpha^2} \quad (2).$$

The relationship between depth resolution and the capability of atomic-resolution STEM imaging of samples embedded in EC media is a main concern in this review and will be discussed in the next section.

When incident electrons interact with a material, resolution deteriorates because of elastic and inelastic scattering, as given by:

$$d_{xy}' = \sqrt{\left(d_{xy}\right)^2 + (d_{blur})^2 + (d_{SNR})^2} \quad (3),$$

where the chromatic aberration term in d_{xy} increases with inelastic scattering. d_{blur} is probe blurring (broadening) due to elastic scattering as given by [22, 25]:

$$d_{blur} = \frac{\lambda^2}{2\pi a_H} t^{1.5} \sqrt{\frac{N_A \rho}{3\pi W}} Z(1 + E/E_0) \quad (4)$$

where a_H is the Bohr radius, t is the thickness of the material, N_A is Avogadro's number, ρ is the mass density, W is the atomic weight, Z is the atomic number, E_0 is electron rest energy.

d_{SNR} is the resolution limited by the signal-to-background ratio, which is synonymous with the signal-to-noise ratio (SNR). Here, we consider the case of a small particle with thickness (diameter) t_s embedded in a matrix with thickness t_m. Chromatic aberration and beam blurring can be minimized when the particle sample is located at the entrance surface of the matrix. However, d_{SNR} is affected by the matrix, independent of the sample depth. In conventional STEM, where the vertical dimension of the probe is comparable to or larger than the matrix, an image of the sample in the media is given by a simple 2D linear imaging model [10]. Hence, the scattering cross-sections of the materials and their thicknesses determine the image contrast. N_{signal}, the number of electrons scattered by the sample and collected with an annular dark-field (ADF) detector, and N_{bkg}, the ADF background signal without the sample, are given by [25-30]:

$$N_{signal} = N_0 \left\{1 - exp\left[-\left(\frac{t_s}{l_s} + \frac{t_m}{l_m}\right)\right]\right\} \quad (5)$$

$$N_{bkg} = N_0 \left\{1 - exp\left[-\left(\frac{t_m}{l_m}\right)\right]\right\} \quad (6),$$

where N_0 is the number of incident electrons, and l_s and l_m are the elastic scattering mean-free-path lengths for the sample and the matrix, respectively [25,28]. This is given by:

$$l(\beta) = \frac{W}{\sigma(\beta)\rho N_A} \quad (7)$$

where β is the maximum scattered angle of the inner region of the ADF detector, and $\sigma(\beta)$ is the elastic scattering cross-section. According to the Rose criteria, the sample particle in the matrix is visible when the SNR is greater than 3–5, as follows [22-23, 25, 29-31]:

$$SNR = \frac{N_{signal} - N_{bkg}}{\sqrt{N_{bkg}}} \geq 3\sim5 \quad (8).$$

Hence, d_{SNR} is regarded as the size (t_s) that satisfies the above condition and is the resolution for a sample embedded in a thick matrix. This simple 2D linear imaging model is useful when the vertically elongated STEM probe is larger than the matrix thickness. However, it is no longer valid for depth-sectioning STEM with a vertical probe size that is significantly less than the matrix thickness. A 3D linear imaging model that provides images via convolution of a 3D PSF and a 3D object function must be adopted to provide sample contrast in a thick matrix.

3D characteristics of depth-sectioning STEM

Figure 1a shows simulated images of probe cross-sections for a conventional STEM with C_s=1.0 mm and α=10 mrad, and an aberration-corrected STEM with C_s=0 mm and α= 28 mrad, in which chromatic aberration and partial coherency are not included. The cross-section of the aberration-corrected probe (i.e., PSF) exhibits an X-shape, and the intensity on the xy-plane, apart from the in-focus position, is low. The intensity profile along the z-direction is approximated by a Gaussian, where the depth resolution can be defined as the full-width at half-maximum, which is about 2.4 times that of the standard deviation. Hence, the HAADF intensity is proportional to the number of electrons hitting an object at the in-focus position, and decreases as the out-of-focus value increases, as shown in Fig. 1b.

It is qualitatively understood that the X-shaped probe results in the dependency of 3D contrast transfer characteristics on frequency components in the lateral plane. Xin et al. investigated the 3D characteristics of aberration-corrected STEM depth-sectioning, as well as other 3D imaging techniques such as hollow-cone ADF-STEM and scanning confocal electron microscopy (SCEM) [32]. Their 3D imaging reconstructions were convolutions of a probe (3D PSF) and a sample (3D object function), and were demonstrated via simulation and experiment. Figure 2 shows analytically calculated CTF boundaries showing contrast-transferable frequency limits for (a) a bright-field (BF)-STEM/TEM, (b) a hollow-cone illuminated ADF-STEM, (c) an ADF-STEM and a coherent BF-SCEM, and (d) an incoherent SCEM. Figure 3b-f shows 3D reconstructions calculated via convolution of the PSFs for the above imaging modes and the model object in Fig. 3a. The BF-STEM transferred depth information only on the two parabolic surfaces of $k_z=\pm 0.5\lambda k_r^2$, and transferable depth information for hollow-cone illumination ADF-STEM was worse than that of ADF-STEM, despite the high-tilt beam illumination. Maximum resolution is obtained at a point that results in the highest lateral resolution, but there is a missing cone that depends on a convergence semi-angle α. Hence, depth resolution depends on the lateral frequency, and decreases at lower frequencies. Because the lateral probe size of aberration-corrected STEM is comparable to an atom or less, depth-sectioning by aberration-corrected STEM is the most powerful way to observe 3D atomic structure in a matrix.

Lastly, SCEM is a unique mode in 3D STEM imaging [32-42], and, if the signals are incoherent, the CTF analytic boundary in the low-frequency range becomes flat and the missing cone is filled, as shown in Fig. 2d. Difficulties of SCEM are that it requires special tuning of probe-forming and imaging-lens correctors, and it suffers from the very low number of signals passing through the small pinhole.

Thus, depth-sectioning STEM with an aberration-corrected atomic-size probe can enhance image intensities of atoms or atomic columns at specific depths because of the CTF 3D characteristics. d_{SNR} could be improved, even for a sample embedded in a thick matrix. If the sample is positioned close to the entrance surface side of the matrix, d_{blur} and d_{SNR} in Eq. (3) are reduced and atomic-structure imaging is possible. Similarly, depth-sectioning STEM is capable of atomic-structural imaging of samples in EC with gas and liquid media.

Applications of depth-sectioning STEM

Atomic-scale depth-position analysis for thin crystalline films

In the early development of depth-sectioning STEM, 3D visualizations of metal nanoparticles on oxide supports and single atoms in an amorphous layer were demonstrated with a probe having α=23 mrad [4-6, 32]. Figure 4a shows a through-focal series of HAADF-STEM images of a single Hf atom in an amorphous SiO_2 layer. The Hf atom location could be determined with sub-Angstrom lateral and 6–7-nm vertical resolutions, demonstrating that detection of single atoms in a matrix with a high SNR was possible via depth-sectioning STEM [4]. It has been used to determine 3D distributions of isolated dopant atoms in semiconductor and ceramic thin films with thicknesses comparable to the vertical size of the beam [11-13, 16]. In these crystalline materials, incident electrons are modulated by channeling effects along crystallographic zone axes. Therefore, the observed depth positions of hetero-element atoms embedded in a crystalline matrix differ from actual positions, which require image simulations incorporating dynamical scattering for correction [3, 7-18]. Figure 4b shows 3D characterization of single Ce dopant atoms in wurtzite-type AlN via depth-sectioning STEM; the Ce depth from the AlN entrance surface was determined with unit-cell precision by combining quantitative STEM imaging and simulating the dependence of the HAADF signal on the Ce depth in the atomic column [12]. 70-mrad α enabled 3D distributions of single Ce dopant atoms in cubic BN viewed along the [110] orientation, obtained from a focal series of STEM images with 2.14-nm depth resolution [16], as well as the determination of the surface atomic topography of a SrTiO3 single-crystal thin film, as shown in Fig. 4e, that was reconstructed from the focus-averaged HAADF-STEM image in Fig. 4d [18].

In contrast to amorphous samples in which the depth resolution simply decreases with thickness increases, channeling in crystalline samples modulates the vertical distribution of dopants in atomic columns, making 3D distribution characterizations difficult. However, the channeling-induced beam confinement along atomic columns enhances the image intensity at atomic columns. Therefore, the combination of 3D depth-sectioning STEM and channeling-induced intensity enhancement of atomic columns makes it possible to image atomic structures of samples in thick matrices. The enhancement is particularly prominent when the sample is located at the entrance surface side and the incident orientation is on the crystallographic zone axis.

EC-STEM observations in air and water

Observations of samples in gas and liquid media in an EC involve similar depth-sectioning STEM technique used for samples embedded in amorphous matrices. Figure 5 shows examples of aberration-corrected EC-STEM depth-sectioning imaging of Pt nanowire networks in air, which were obtained through 30-nm-thick silicon nitride EC windows [20]. The sample was deposited on the inner surface of the top window, and the elapsed time is displayed at the bottom right of each image. Atomic columns in the grains were intense bright dots, demonstrating atomic structure imaging in an EC, especially when the crystallographic orientations were aligned with the beam axis. Three grains were connected with their {111} planes, and the atomic structure change in the central region of each grain was less than that on the surfaces and grain boundaries (GBs). Atoms on the surfaces and GBs continued fluctuating in Fig. 5a-c, where surface atoms randomly appeared and disappeared, while surface growth and etching due to atomic step motions were not observed. From the detailed analysis, the Pt {111} surfaces were oxidized, which might hinder surface atomic diffusion and weaken changes in the sizes of the grains and GBs. Hence, morphology changes of the Pt network in air were mainly attributed to deformation and movement of chain-connected grains and GBs, but not step motion induced by surface atomic diffusion.

Figure 6 shows the same Pt nanowire network sample that was then embedded in ultra-thin water layers in the EC. Small isolated fragments rapidly moved around, while the network chains slowly changed the shape. Many fragments moved around three-dimensionally by jumping over the Pt networks. For example, fragments indicated by arrows 1 and 2, not seen in Fig. 6a, suddenly appeared in Fig. 6b and then disappeared in Fig. 6c. Meanwhile, regions of the chains indicated by arrows 3 and 4 were deformed and disconnected, and the region indicated by arrow 5 seemed to have peeled off and tilted. Although the chain deformation speed increased with magnification, the atomic structure could be resolved in some regions of the networks, as shown in Fig. 7. The deformation speed of the network in water was faster than that in air, while morphology changes were the same. An arrowhead shows the change in GB atomic structures in Fig. 7a,b. This atomic reconstruction relaxed the strain energy in both air and water. However, no surface oxide layer was formed. This may have been because H_2 molecules produced from electron-beam-induced H_2O radiolysis reduced the Pt oxide.

Figure 8 shows a depth-sectioning EC-STEM of Pt nanoparticles in ultra-thin water imaged via [43]. At the beginning of medium magnification STEM imaging, some small nanoparticles disappeared, while others grew larger via Ostwald ripening. Afterward, no significant changes in the nanoparticle density occurred. However, immediately after the beam dose rate was increased by increasing the magnification, the Pt nanoparticles started aggregating because of charge accumulation locally on the membrane in the area irradiated by the intense beam. Atomic-resolution imaging indicated that the particles were likely to bind to each other via their {111} surfaces. This oriented attachment was consistent with previous reports [44].

Summary and outlook

Many factors must be considered when using (S)TEM to understand atomic-level dynamic phenomena that occur in samples in air and liquid media. Atomic resolution is one of the most critical issues, and depth-sectioning STEM is a promising method. Aberration correction technology in electron microscopy has enabled lateral and vertical resolutions at atomic and nanometer scales, respectively. The latter enables us to perform practical depth-sectioning in STEM and enhances the SNR of the sample in the presence of silicon nitride membranes and media. This leads to atomic-resolution EC-STEM. Graphene is an ideal material for high-resolution EC-(S)TEM because it provides a high SNR by its low atomic number and extreme thinness. The most popular graphene EC is thin liquid pockets sandwiched with two graphene sheets [45-47]. However, the applications are limited because it is hard to survive against intense electron irradiation for a long exposure time. The poor extensibility is also an issue, but some extension initiatives have been made, such as microwell [48-50] and liquid-flow graphene ECs [51]. Single atoms in liquid were observed by combining a micro-well graphene EC with aberration-corrected STEM depth-sectioning [50].

Another important issue is electron-beam-induced radiolysis. Radiolysis products that induce chemical reactions with a sample will be significant if the dose rate increases when the magnification increases. In a liquid environment, the formation of radiolysis product gas bubbles in an EC can also be a significant problem because they are likely to affect sample dynamics, solid-liquid reactions, and bulges in membrane windows. To reduce the dose rate, HAADF-STEM is preferable to conventional TEM because HAADF-STEM Z-contrast imaging is more advantageous than TEM phase-contrast imaging with respect to sample SNR, especially for large-atomic-number materials. New types of phase-contrast STEM, such as integrated differential phase-contrast (iDPC) STEM [52-54], optimum BF STEM [55], and STEM ptychography [56, 57], can significantly improve the SNR, thereby reducing the dose rate by two orders of magnitude. iDPC-STEM and STEM ptychography have been adopted for low-dose cryo-EM single-particle analysis of biological samples embedded in ice [51, 56]. Dose-rate control such as electron dose modulation via pulse illumination in TEM and STEM eliminates unnecessary electrons and enables minimum sample doses [58]. Random and alternative scans of a STEM beam can also reduce the accumulation of radiolysis products as well as sample damage [59-61]. The most significant disadvantage of STEM is insufficient temporal resolution because of limited beam scan speeds. In response to this challenge, Ishikawa et al. developed a 25 frames/s scanning system [62].

The combination of aberration-corrected STEM depth-sectioning with the constant development of advanced technologies such as low-dose, high-contrast, and high-speed scanning systems has enabled further high-spatial and -temporal imaging of dynamics of materials in gas and liquid environments.

Acknowledgements

We thank Drs. Li X and Takei T for helpful discussion. We thank Edanz (https://jp.edanz.com/ac) for editing a draft of this manuscript.

Funding

A part of this work was supported by Innovative Science and Technology Initiative for Security, Acquisition, Technology & Logistics Agency (ATLA), Japan (No. JPJ004596), and the Adaptable and Seamless Technology Transfer Program, A-STEP, Japan Science and Technology Agency (JST), Japan (No. JPMJTM20KU).

AH thanks financial supports by Precursory Research for Embryonic Science and Technology (PRESTO) [No. JPMJPR17S7], Japan Science and Technology Agency (JST), and Grant-in-Aid for Scientific Research (C) (KAKENHI) [No. 21K05248], Japan Society for the Promotion of Science (JSPS).

Data Availability Statements

Not applicable.

Conflict of Interest

The authors declare that they have no conflict of interest.

References

1. Hovden R, and Muller D A (2022) Electron tomography for functional nanomaterials. MRS Bulletin 45: 298-304. https://doi.org/10.1557/mrs.2020.87
2. Baba N, Hata S, Saito H, and Kaneko K (2023) Three-dimensional electron tomography and recent expansion of its applications in materials science. Microscopy 72: 111-134. https://doi.org/10.1093/jmicro/dfac071
3. Peng Y, Nellist P D, and Pennycook S J (2004) HAADF-STEM imaging with sub-angstrom probes: a full Bloch wave analysis. J. Electron Microsc. 53: 257-266. https://doi.org/10.1093/jmicro/53.3.257
4. van Benthem K, Lupini A R, Kim M, Baik H S, Doh S, Lee J, Oxley M P, Findlay S D, Allen L J, Luck J T, and Pennycook S J (2005) A three-dimensional imaging of individual hafnium atoms inside a semiconductor device. Appl. Phys. Lett. 87: 034104. https://doi.org/10.1063/1.1991989
5. van Benthem K, Lupini A R, Oxley M P, Findlay S D, Allen L J, and Pennycook S J (2006) Three-dimensional ADF imaging of individual atoms by through-focal series scanning transmission electron microscopy. Ultramicroscopy 106: 1062-1068. https://doi.org/10.1016/j.ultramic.2006.04.020
6. Borisevich A Y, Lupini A R, and Pennycook S J (2006) Depth sectioning with the

aberration-corrected scanning transmission electron microscope. Proc. Natl. Acad. Sci. USA 103: 3044-3048. https://doi.org/10.1073/pnas.0507105103

7. Borisevich A Y, Lupini A R, Travaglini S, and Pennycook S J (2006) Depth sectioning of aligned crystals with the aberration-corrected scanning transmission electron microscope. J. Electron Microsc. 55: 7–12. https://doi.org/10.1093/jmicro/dfi075
8. Cosgriff E C, and Nellist P D (2007) A Bloch wave analysis of optical sectioning in aberration-corrected STEM. Ultramicroscopy 107: 626-634. https://doi.org/10.1016/j.ultramic.2006.12.004
9. D'Alfonso A J, Findlay S D, Oxley M P, and Pennycook S J (2007) Depth sectioning in scanning transmission electron microscopy based on core-loss spectroscopy. Ultramicroscopy 108: 17-28. https://doi.org/10.1016/j.ultramic.2007.02.026
10. Xin H L, Intaraprasonk V, and Muller D A (2008) Depth sectioning of individual dopant atoms with aberration-corrected scanning transmission electron microscopy. Appl. Phys. Lett. 92: 013125. https://doi.org/10.1063/1.2828990
11. Hwang J, Zhang J Y, D'Alfonso A J, Allen L J, and Stemmer S (2013) Three-dimensional

imaging of individual dopant atoms in SrTiO3. Phys. Rev. Lett. 111: 266101. https://doi.org/10.1103/PhysRevLett.111.266101

12. Ishikawa R, Lupini A R, Findlay S D, Taniguchi T, and Pennycook S J (2014) Three-dimensional location of a single dopant with atomic precision by aberration-corrected scanning transmission electron microscopy. Nano. Lett. 14: 1903–1908. https://doi.org/10.1021/nl500564b
13. Ishikawa R, Lupini A R, Findlay S D, Hinuma Y, and Pennycook S J (2015) Large-angle illumination STEM: Toward three-dimensional atom-by-atom imaging. Ultramicroscopy 151: 122-129. https://doi.org/10.1016/j.ultramic.2014.11.009
14. Hamaoka T, Jao C, Zhang X, Oshima Y, and Takeguchi M (2017) Three-dimensional characterization of Guinier–Preston zones in an Al–Cu alloy using depth-sectioning technique. Microscopy 66: 78-88. https://doi.org/10.1093/jmicro/dfw104
15. Bosch E G T, and Lazić I (2019) Analysis of depth-sectioning STEM for thick samples and 3D imaging. Ultramicroscopy 207: 112831. https://doi.org/10.1016/j.ultramic.2019.112831
16. Ishikawa R, Shibata N, Taniguchi T, and Ikuhara Y (2020) Three-dimensional imaging of a single dopant in a crystal. Phys. Rev. Appl. 13: 034064.

https://doi.org/10.1103/PhysRevApplied.13.034064

17. Ishizuka A, Ishizuka K, Ishikawa R, Shibata N, Ikuhara Y, Hashiguchi H, and Sagawa R (2021) Improving the depth resolution of STEM-ADF sectioning by 3D deconvolution. Microscopy 70: 241–249. https://doi.org/10.1093/jmicro/dfaa056
18. Ishikawa R, Tanaka R, Kawahara K, Shibata N, and Ikuhara Y (2021) Atomic-resolution topographic imaging of crystal surfaces. ACS Nano 15: 9186–9193. https://doi.org/10.1021/acsnano.1c02907
19. Ohsuna T, and Oh-ishi K (2023) Model-based deconvolution for particle analysis applied to a through-focus series of HAADF-STEM images. Microscopy 72: 368–380. https://doi.org/10.1093/jmicro/dfac070
20. Takeguchi M, Takei T, and Mitsuishi K (2023) The atomic observation of the structural change process in Pt networks in air using environmental cell scanning transmission electron microscopy. Nanomaterials 13: 2170. https://doi.org/10.3390/nano13152170
21. Hashimoto A, Shimojo M, Mitsuishi K, and Takeguchi M (2010) Three-dimensional optical sectioning by scanning confocal electron microscopy. Microsc. Microanal. 16: 233-238. https://doi.org/10.1017/S1431927610000127

22. Reimer L, and Kohl L (2008) Transmission Electron Microscopy (Springer New York, New York).
https://doi.org/10.1007/978-0-387-40093-8

23. Tanaka N (2014) Scanning Transmission Electron Microscopy of Nanomaterials (Imperial College Press, London).
http:// doi.org/10.1142/p807

24. Born M, and Wolf E (1999) Principles of Optics (Cambridge University Press, Cambridge).
https://doi.org/10.1017/CBO9781139644181

25. de Jonge N (2018) Theory of the spatial resolution of (scanning) transmission electron microscopy in liquid water or ice layers. Ultramicroscopy 187: 113-125.
https://doi.org/10.1016/j.ultramic.2018.01.007

26. de Jonge N, Peckys D B, Kremers G J, and, and Piston D W (2009) Electron microscopy of whole cells in liquid with nanometer resolution. Proc. Natl. Acad. Sci. USA 106: 2159-2164.
https://doi.org/10.1073/pnas.0809567106

27. Demers H, Poirier-Demers N, Drouin D, and de Jonge N (2010) Simulating STEM imaging of nanoparticles in micrometers-thick substrates. Microsc. Microanal. 16: 795-804.

https://doi.org/10.1017/S1431927610094080

28. de Jonge N, and Ross F (2011) Electron microscopy of specimens in liquid. Nat. Nanotechol. 6: 695–704. https://doi.org/10.1038/nnano.2011.161
29. Zulfiqar A, Azim S, Ortega E, and de Jonge N (2022) Automated calculations for computing the sample-limited spatial resolution in (scanning) transmission electron microscopy. Ultramicroscopy 242: 113611. https://doi.org/10.1016/j.ultramic.2022.113611
30. de Jonge N, Verch A, and Demers H (2018) The influence of beam broadening on the spatial resolution of annular dark field scanning transmission electron microscopy. Microsc. Microanal. 24: 8-16. https://doi.org/10.1017/S1431927618000077
31. Rose A (1973) Vision (Springer New York, New York). https://doi.org/10.1007/978-1-4684-2037-1
32. Xin H L, and Muller D A (2009) Aberration-corrected ADF-STEM depth sectioning and prospects for reliable 3D imaging in S/TEM. J. Electron Microsc. 58: 157-165. https://doi.org/10.1093/jmicro/dfn029
33. Nellist P D, Behan G, Kirkland A I, and Hetherington C J D (2006) Confocal operation of a transmission electron microscope with two aberration correctors. Appl. Phys. Lett. 89:

124105.

https://doi.org/10.1063/1.2356699

34. Takeguchi M, Hashimoto A, Shimojo M, Mitsuishi K, and Furuya K (2008) Development of a stage-scanning system for high-resolution confocal STEM. J. Electron Microsc. 57: 123-127.

    https://doi.org/10.1093/jmicro/dfn010

35. Hashimoto A, Shimojo M, Mitsuishi K, and Takeguchi M (2009) Three-dimensional imaging of carbon nanostructures by scanning confocal electron microscopy. J. Appl. Phys. 106: 086101.

    https://doi.org/10.1063/1.3225103

36. Hashimoto A, Shimojo M, Mitsuishi K, and Takeguchi M (2010) Three-dimensional optical sectioning by scanning confocal electron microscopy with a stage-scanning system. Microsc. Microanal. 16: 233–238.

    https://doi.org/10.1017/S1431927610000127

37. Wang P, Behn G, Takeguchi M, Hashimoto A, Mitsuishi K, Shimojo M, Kirkland A I, and Nellist P D (2010) Nanoscale energy-filtered scanning confocal electron microscopy using a double-aberration-corrected transmission electron microscope. Phys. Rev. Lett. 104: 200801.

    https://doi.org/10.1103/PhysRevLett.104.200801

38. Hashimoto A, Wang P, Shimojo M, Mitsuishi K, Nellist P D, Kirkland A I, and Takeguchi (2012) Three-dimensional analysis of nanoparticles on carbon support using aberration-corrected scanning confocal electron microscopy. Appl. Phys. Lett. 101: 253108. https://doi.org/10.1063/1.4772514

39. Zhang X, Takeguchi M, Hashimoto A, Mitsuishi K, Wang P, Nellist P D, Kirkland A I, Tezuka M, and Shimojo M (2012) Three-dimensional observation of SiO_2 hollow spheres with a double-shell structure using aberration-corrected scanning confocal electron microscopy. J. Electron Microsc. 61: 159-169. https://doi.org/10.1093/jmicro/dfs039

40. Wang P, Hashimoto A, Takeguchi M, Mitsuishi K, Shimojo M, Zhu Y, Okuda M, Kirkland A I, and Nellist P D (2012) Three-dimensional elemental mapping of hollow Fe_2O_3@SiO_2 mesoporous spheres using scanning confocal electron microscopy. Appl. Phys. Lett. 100: 213117.

https://doi.org/10.1063/1.4714889

41. Wang P, D’Alfonso A J, Hashimoto A, Morgan A J, Takeguchi M, Mitsuishi K, Shimojo M, Kirkland A I, Allen L J, and Nellist P D (2013) Contrast in atomically resolved EF-SCEM imaging. Ultramicroscopy 134: 185-192. https://doi.org/10.1016/j.ultramic.2013.06.007

42. Hamaoka T, Hashimoto A, Mitsuishi K, and Takeguchi M (2018) 4D-data acquisition in

scanning confocal electron microscopy for depth-sectioned imaging. e-J. Surf. Sci. Nanotechnol. 16: 247-252. https://doi.org/10.1380/ejssnt.2018.247

43. Takeguchi M, Li X, and Mitsuishi K (2022) High-resolution STEM observation of the dynamics of Pt nanoparticles in a liquid. Jpn. J. Appl. Phys. 61: SD1021. https://doi.org/10.35848/1347-4065/ac54f0
44. Zhu C, Liang S, Song E, Zhou Y, Wang W, Shan F, Shi Y, Hao C, Yin K, Zhang T, Liu J, Zheng H, and Sun L (2018) In-situ liquid cell transmission electron microscopy investigation on oriented attachment of gold nanoparticles. Nat Commun 9: 421. https://doi.org/10.1038/s41467-018-02925-6
45. Yuk J, Park J, Ercius P, Kim K, Hellebusch D J, Crommie M F, Lee J, Zettl A, and Alivisatos A P (2012) High-Resolution EM of Colloidal Nanocrystal Growth Using Graphene Liquid Cells. Science 336: 61-64. https://doi.org/10.1126/science.1217654
46. Park J, Koo K, Noh N, Chang J H, Cheong J Y, Dae K S, Park J S, Ji S, Kim I, and Yuk J M (2021) Graphene Liquid Cell Electron Microscopy: Progress, Applications, and Perspectives. ACS Nano 2021, 15, 288–308 https://doi.org/10.1021/acsnano.0c10229
47. Sung J, Bae Y, Park H, Kang S, Choi B K, Kim J, and Park J (2022) Liquid-Phase

Transmission Electron Microscopy for Reliable In Situ Imaging of Nanomaterials. Annu. Rev. Chem. Biomol. Eng. 13: 167-191. https://doi.org/10.1146/annurev-chembioeng-092120-034534

48. Hutzler A, Schmutzler T, Jank M P M, Branscheid R, Unruh T, Spiecker E, and Frey L (2018) Unravelling the Mechanisms of Gold–Silver Core–Shell Nanostructure Formation by in Situ TEM Using an Advanced Liquid Cell Design. Nano Lett. 18: 7222–7229. https://doi.org/10.1021/acs.nanolett.8b03388
49. Lim K, Bae Y, Jeon S, Kim K, Kim B H, Kim J, Kang S, Heo T, Park J, and Lee W C (2020) A Large-Scale Array of Ordered Graphene-Sandwiched Chambers for Quantitative Liquid-Phase Transmission Electron Microscopy. Adv. Mater. 32: 2002889. https://doi.org/10.1002/adma.202002889
50. Clark N, Kelly D J, Zhou M, Zou Y, Myung C W, Hopkinson D G, Schran C, Michaelides A, Gorbachev R, and Haigh S J (2022) Tracking single adatoms in liquid in a transmission electron microscope. Nature 609: 942–947. https://doi.org/10.1038/s41586-022-05130-0
51. Koo K, Park J, Ji S, Toleukhanova S, and Yuk J M (2021) Liquid-Flowing Graphene Chip-Based High-Resolution Electron Microscopy. Adv, Mater. 33: 2005468. https://doi.org/10.1002/adma.202005468
52. Lazić I, Wirix M, Leo Leidl M, de Haas F, Mann D, Beckers M, V. Pechnikova E, Müller-

Caspary K, Egoavil R, G. T. Bosch E, and Sachse C (2022) Single-particle cryo-EM structures from iDPC–STEM at near-atomic resolution. Nat. Methods 19: 1126-1136. https://doi.org/10.1038/s41592-022-01586-0

53. Song D, Zhang X, Lian C, Liu H, Alexandrou I, Lazić I, G. T. Bosch E, Zhang D, Wang L, Yu R, Cheng Z, Song C, Ma X, Duan W, Xue Q, Zhu J (2019) Visualization of dopant oxygen atoms in a $Bi_2Sr_2CaCu_2O_{8+\delta}$ Superconductor. Adv. Funct. Mater. 29: 1903843. https://doi.org/10.1002/adfm.201903843

54. Shen B, Chen X, Wang H, Xiong H, G. T. Bosch E, Lazić I, Cai D, Qian W, Jin S, Liu X, Han Y, and Wei F (2021) A single-molecule van der Waals compass. Nature 592: 541–544. https://doi.org/10.1038/s41586-021-03429-y

55. Ooe K, Seki T, Yoshida K, Kohno Y, Ikuhara Y, and Shibata N (2021) Direct imaging of local atomic structures in zeolite using optimum bright-field scanning transmission electron microscopy. Sci. Adv. 9: eadf686. https://doi.org/10.1126/sciadv.adf6865

56. Lozano J G, Martinez G T, Jin L, Nellist P D, and Bruce P. G. (2018) Low-dose aberration-free imaging of Li-rich cathode materials at various states of charge using electron ptychography. Nano Lett. 18: 6850–6855. https://doi.org/10.1021/acs.nanolett.8b02718 (2018)

57. Pei X, Zhou L, Huang C, Boyce M, S. Kim J, Liberti E, Hu Y, Sasaki T, Nellist P D,

Zhang P, Stuart D I, Kirkland A I, and Wang P (2023) Cryogenic electron ptychographic single particle analysis with wide bandwidth information transfer. Nat. Commun. 14: 3027.
https://doi.org/10.1038/s41467-023-38268-0

58. Reed B W, Bloom R S, Eyzaguirre G, Henrichs C, Moghadam A A, and Masiel D J (2022) Electrostatic switching for spatiotemporal dose control in a transmission electron microscope. Microsc. Microanal. 28: 2230–2231.
https://doi.org/10.1017/S1431927622008595
59. Zobelli A, Woo S Y, Tararan A, Tizei L H G, Brun N, Li X, Stéphan O, Kociak M, and Tencé M (2020) Spatial and spectral dynamics in STEM hyperspectral imaging using random scan patterns. Ultramicroscopy 212: 112912.
https://doi.org/10.1016/j.ultramic.2019.112912
60. Velazco A, Béché A, Jannis D, and Verbeeck J (2022) Reducing electron beam damage through alternative STEM scanning strategies, Part I: Experimental findings. Ultramicroscopy 232: 113398.
https://doi.org/10.1016/j.ultramic.2021.113398
61. Jannis D, Velazco A, Béché A, and Verbeeck J (2022) Reducing electron beam damage through alternative STEM scanning strategies, Part II: Attempt towards an empirical model describing the damage process. Ultramicroscopy 240: 113568.

https://doi.org/10.1016/j.ultramic.2022.113568

62. Ishikawa R, Jimbo Yu, Terao M, Nishikawa M, Ueno Y, Morishita S, Mukai M, Shibata N, Ikuhara Y (2020) High spatiotemporal-resolution imaging in the scanning transmission electron microscope. Microscopy 69: 240-247 https://doi:org/10.1093/jmicro/dfaa017.

Figure Legends

Fig. 1 (a) Simulated images of probe cross-sections for conventional scanning transmission electron microscopy (STEM) with C_s=1 mm and α=10 mrad (left), and aberration corrected STEM with C_s=0 mm and α=28 mrad (right). (b) Positional relationships between an object and STEM probes with N_0 electrons for different focus conditions.

Fig. 2 (a) Schematic analytical boundaries of contrast transfer functions for (a) bright-field (BF)-scanning transmission electron microscopy (STEM)/TEM, (b) hollow-cone illuminated annular dark-field (ADF)-STEM, (c) ADF-STEM and coherent BF-scanning confocal electron microscopy (SCEM), and (d) incoherent SCEM.

Reprinted with permission from [32]

Fig. 3 (a) Cross-section of an object used for 3D reconstruction calculations of (b-f). (b-f) Cross-sections of 3D reconstructions (b) bright-field (BF)-scanning transmission electron microscopy (STEM)/TEM, (c) annular dark-field (ADF)-STEM, (d) hollow-cone ADF-STEM, (e) coherent BF-scanning confocal electron microscopy (SCEM), and (f) incoherent SCEM, calculated from (a).

Reprinted with permission from [32]

Fig. 4 (a) A through-focal series of high-angle annular dark-field (HAADF)-scanning transmission electron microscopy (STEM) images of a single Hf atom in an amorphous SiO_2 layer. (b) HAADF-STEM image of a single Ce atom in wurtzite AlN. (c) A through-focal series of HAADF images of single Ce atoms in cubic BN. (d) A focus-averaged HAADF-STEM image of a $SrTiO_3$ crystal viewed from [001] direction. (e) A surface topography of a $SrTiO_3$ (001), reconstructed from (d).

Subfigures (a), (b), (c), and(d, e) are reprinted with permission from [4], [12], [16], and [18], respectively.

Fig. 5 Environmental cell-scanning transmission electron microscopy images of Pt nanowire networks in air under the electron dose rate of 1.3×10^{-1} pA/nm^2, showing the atomic structural change. The elapsed time is displayed at the bottom right of each image.

Reprinted with permission from [20].

Fig. 6 Environmental cell-scanning transmission electron microscopy images of Pt nanowire networks in water under the electron dose rate of 3.0×10^{-4} pA/nm^2, showing the morphology change. The elapsed time is displayed at the top right of each image.

Fig. 7 Environmental cell-scanning transmission electron microscopy images of Pt nanowire networks in water under the electron dose rate of 1.3×10^{-1} pA/nm^2, showing the atomic structure change. The elapsed time is displayed at the top right of each image.

Fig. 8 Environmental cell-scanning transmission electron microscopy images of Pt nanoparticles in water under the electron dose rate of 8.5×10^{-2} pA/nm^2, showing the aggregation process. The elapsed time is displayed at the top right of each image. Reprinted with permission from [43].

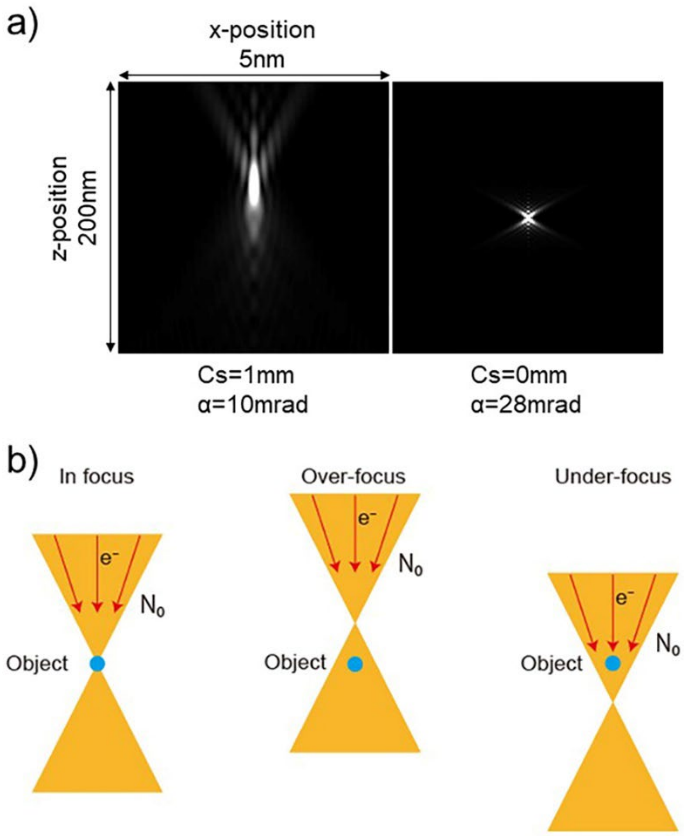
a)
x-position
5nm
z-position
200nm
Cs=1mm
α=10mrad
Cs=0mm
α=28mrad
b)
In focus
Over-focus
Under-focus
e⁻
N₀
Object

Fig. 1

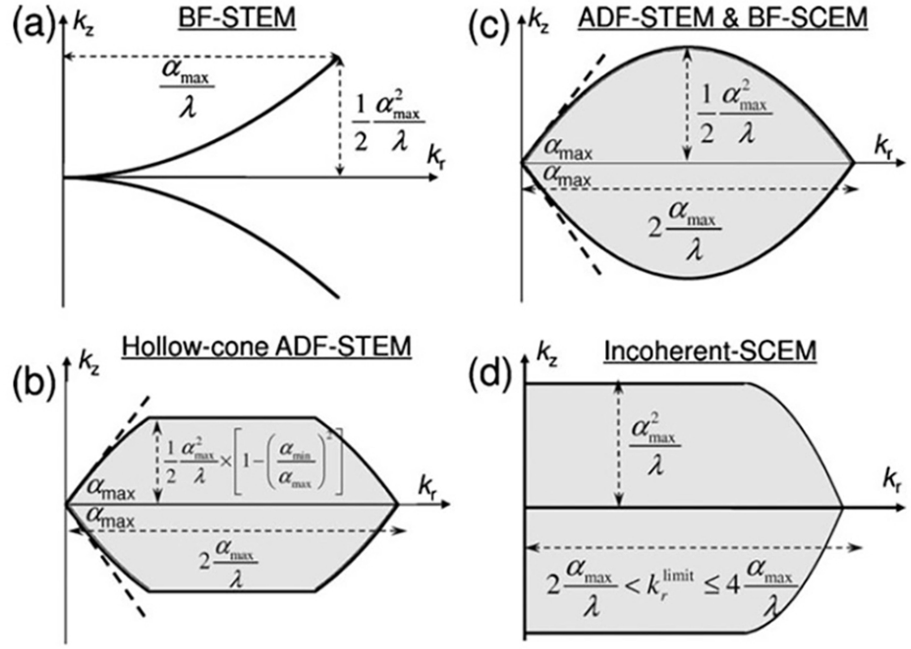
(a)
k_z
BF-STEM
$\frac{\alpha_{\max}}{\lambda}$
$\frac{1}{2}\frac{\alpha_{\max}^2}{\lambda}$
k_r
(c)
k_z
ADF-STEM & BF-SCEM
$\frac{1}{2}\frac{\alpha_{\max}^2}{\lambda}$
k_r
$\alpha_{\max}$
$\alpha_{\max}$
$2\frac{\alpha_{\max}}{\lambda}$
(b)
k_z
Hollow-cone ADF-STEM
$\frac{1}{2}\frac{\alpha_{\max}^2}{\lambda}\times\left[1-\left(\frac{\alpha_{\min}}{\alpha_{\max}}\right)^2\right]$
k_r
$\alpha_{\max}$
$\alpha_{\max}$
$2\frac{\alpha_{\max}}{\lambda}$
(d)
k_z
Incoherent-SCEM
$\frac{\alpha_{\max}^2}{\lambda}$
k_r
$2\frac{\alpha_{\max}}{\lambda} < k_r^{\text{limit}} \le 4\frac{\alpha_{\max}}{\lambda}$

Fig. 2

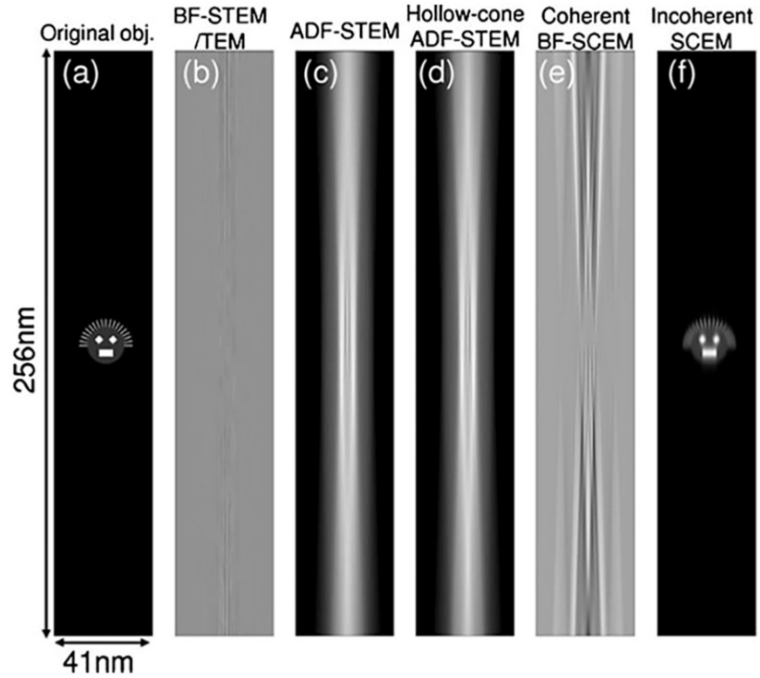
Original obj.
BF-STEM /TEM
ADF-STEM
Hollow-cone ADF-STEM
Coherent BF-SCEM
Incoherent SCEM
(a)
(b)
(c)
(d)
(e)
(f)
256nm
41nm

Fig. 3

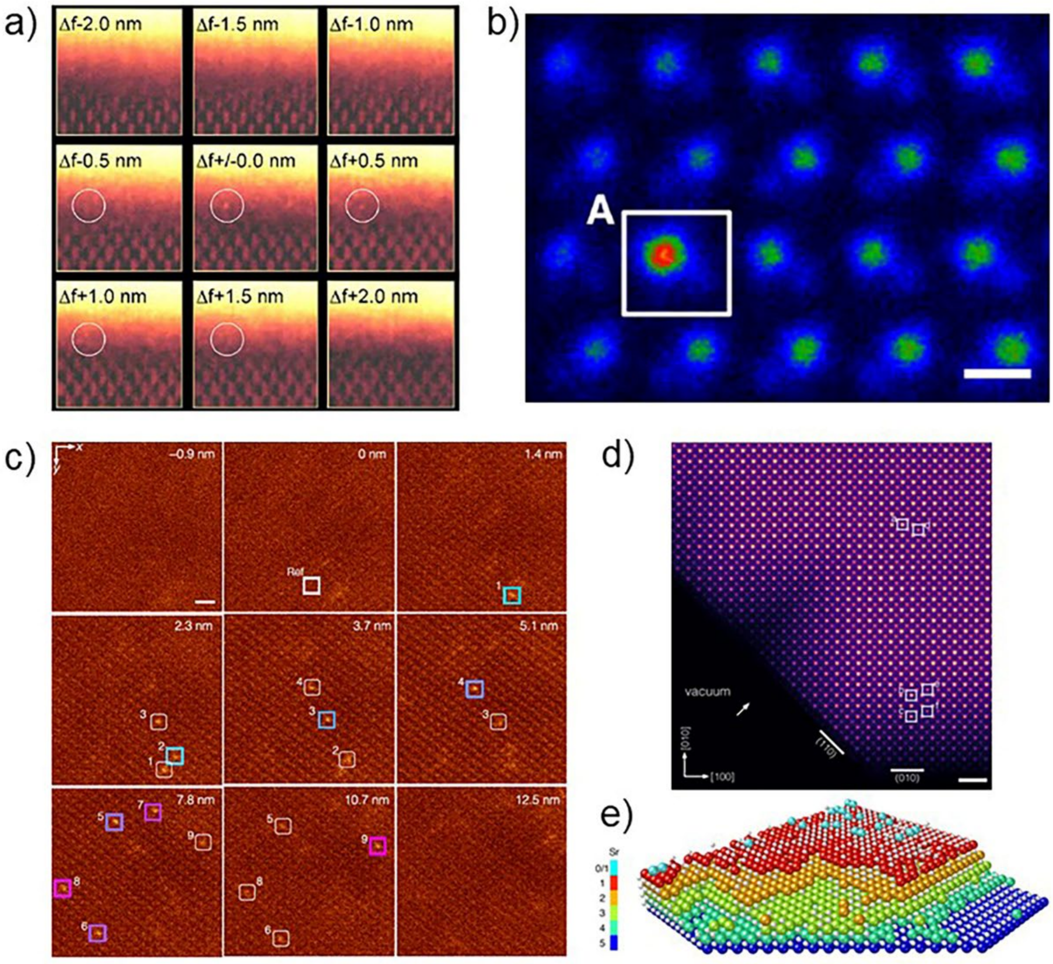
a)
Δf-2.0 nm
Δf-1.5 nm
Δf-1.0 nm
Δf-0.5 nm
Δf+/-0.0 nm
Δf+0.5 nm
Δf+1.0 nm
Δf+1.5 nm
Δf+2.0 nm
b)
A
c)
x
y
−0.9 nm
0 nm
1.4 nm
Ref
2.3 nm
3.7 nm
5.1 nm
7.8 nm
10.7 nm
12.5 nm
1
2
3
4
5
6
7
8
9
d)
vacuum
[010]
[100]
[110]
(010)
e)
Sr
0/1
1
2
3
4
5

Fig. 4

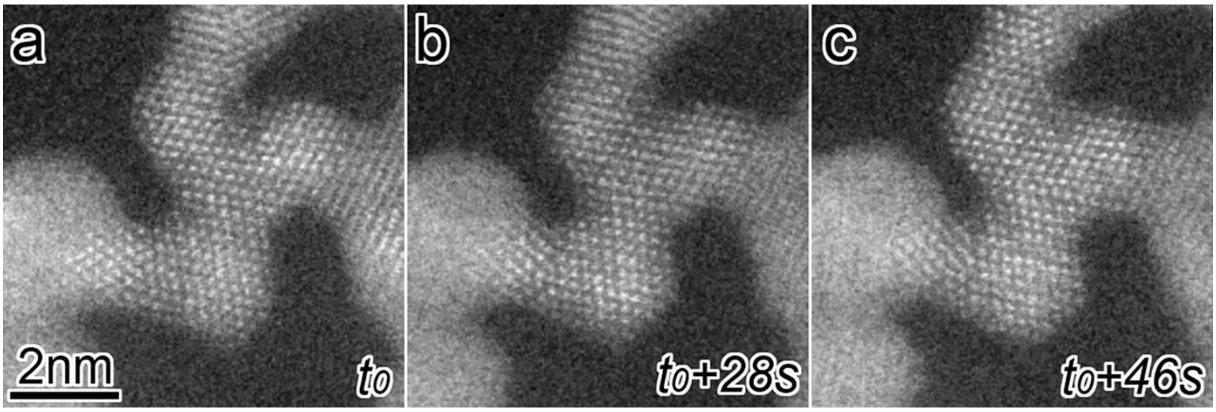

Fig.5

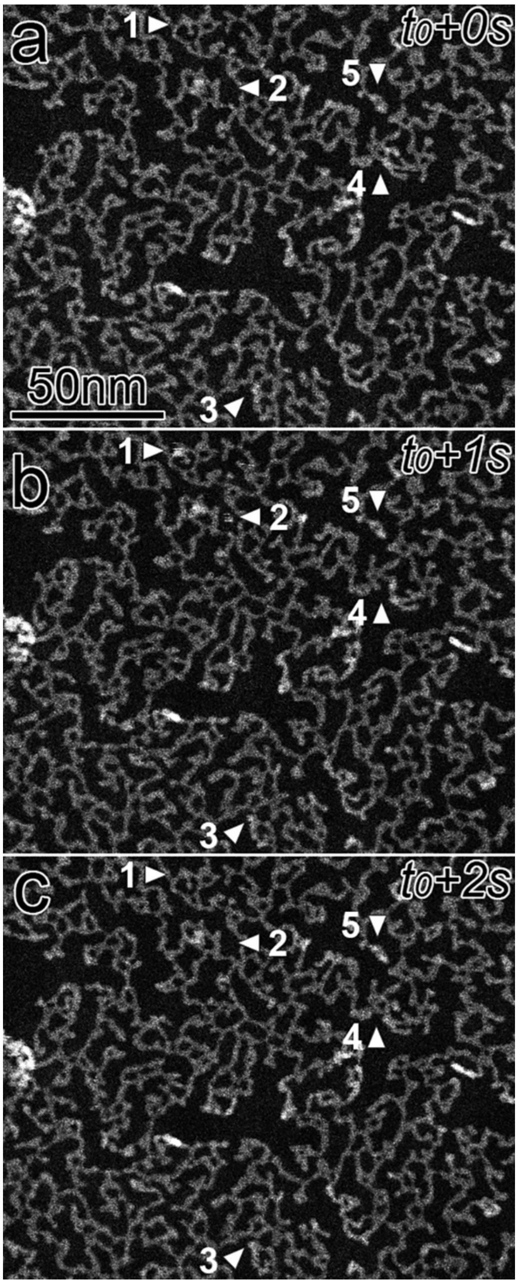

Fig.6

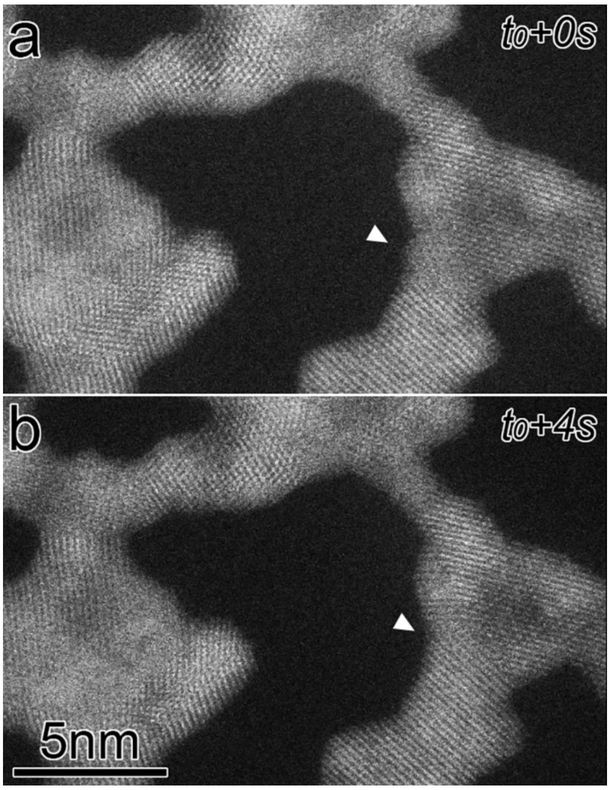

Fig. 7

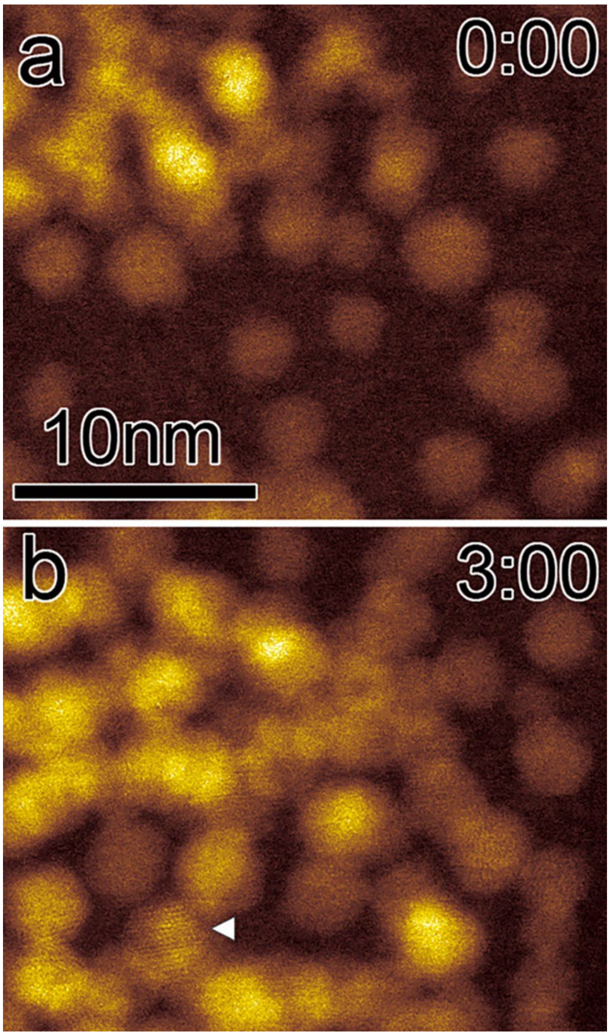

Fig. 8